IEEE Access
Multidisciplinary ⋮ Rapid Review ⋮ Open Access Journal

Received 12 July 2023, accepted 26 July 2023, date of publication 1 August 2023, date of current version 8 August 2023.

Digital Object Identifier 10.1109/ACCESS.2023.3300651

RESEARCH ARTICLE

A Miniaturized Multiband FSS Director Using Double Layer With ICPW Technique Structure for Wireless Communication Systems

P. CHOMTONG[1], (Member, IEEE), N. SOMJIT[2,3,4], (Senior Member, IEEE), P. KRACHODNOK[5], (Member, IEEE), C. MAHATTHANAJATUPHAT[6], (Member, IEEE), S. TAWATCHAI[7], AND P. AKKARAEKTHALIN[6], (Member, IEEE)

[1]Department of Teacher Training in Electrical Engineering, Faculty of Technical Education, King Mongkut's University of Technology North Bangkok, Bangkok 10800, Thailand
[2]School of Electronic and Electrical Engineering, University of Leeds, LS2 9JT Leeds, U.K.
[3]Division of Micro and Nanosystems (MST), KTH Royal Institute of Technology, 114 28 Stockholm, Sweden
[4]Department of Electrical Engineering, Faculty of Engineering, Chiang Mai University, Muang, Chiang Mai 50200, Thailand
[5]School of Telecommunication Engineering, Institute of Engineering, Suranaree University of Technology, Nakhon Ratchasima 30000, Thailand
[6]Department of Electrical and Computer Engineering, Faculty of Engineering, King Mongkut's University of Technology North Bangkok, Bangkok 10800, Thailand
[7]Aeronautical Electronics Engineering from Civil Aviation Training Center (CATC), Bangkok 10900, Thailand

Corresponding authors: N. Somjit (n.somjit@leeds.ac.uk) and P. Akkaraekthalin (prayoot.a@eng.kmutnb.ac.th)

This work was supported in part by the Engineering and Physical Science Research Council under Grant EP/S016813/1, in part by the Swedish Research Council (VR) under Grant 2021-05842_VR, and in part by the King Mongkut's University of Technology North Bangkok under Contract KMUTNB-63-know-025.

ABSTRACT This paper presents a multiband director based on the frequency selective surface (FSS) unit cell structure using the double layer with interdigital CPW (ICPW) technique. The unit cell consists of the front and the back. The front part has been designed using an ICPW technique based on a coplanar waveguide structure to enhance the capacitance between the transmission line and the semi-ground. The overall structural dimension of the unit cell can be designed to be smaller than the conventional range of $\lambda/2$ to $\lambda/8$, due to the influence of the slow wave effect on the capacitance of the structure. The back part is the inverted layer of the front, which alternates between substrate and copper. It is composed of a square loop resonator with a double meandering line. The capacitance generated by a double meander line enhances the capacitance in the front part, which influences the control of all resonant frequencies and increases the slow wave on the double-layer unit cell structure, resulting in a significantly reduced dimension. The resonance frequencies for the designs are 1.8 GHz (LTE), 3.7 GHz (Wi-MAX) and 5.2 GHz (WLAN), respectively. According to simulation results, the FSS can transmit all resonant frequencies. It has an overall dimension of 10.93 mm $\times$ 11.48 mm. In addition, the FSS unit cell has been arranged as a 7×7 array for use as a director. The dimensions are 73.48 mm $\times$ 77.38 mm. The FSS director will be evaluated utilizing an omnidirectional dipole antenna at the same resonant frequency as the FSS unit cell. According to both the simulated and measured outcomes, the impedance matching value is below -10 dB at the three resonant frequencies. The FSS director equipped with a dipole antenna exhibits bidirectional propagation characteristics across all resonant frequencies. The antenna gains for simulation are 3.45 dBi, 3.05 dBi, and 3.72 dBi, while the antenna gains for measurement are 3.05 dBi, 2.98 dBi, and 3.12 dBi. The findings indicate a high level of concurrence.

INDEX TERMS Multiband FSS, interdigital, ICPW, director, coplanar waveguide, capacitive load.

I. INTRODUCTION

Communication is an essential aspect of human existence, particularly wireless communication, which has been

The associate editor coordinating the review of this manuscript and approving it for publication was Hassan Tariq Chattha.

developing continuously and quickly. To meet the rising demand, the wireless communication system has been designed to be small, responsive to a broad spectrum of frequencies, able to support a large quantity of data, possess a long transmission distance, and be inexpensive. During this stage of evolution, a variety of forms have been created. The development of materials frequently occurs concurrently with the creation of a communication system. The material was developed to enhance the efficacy of the wireless communication system. There are numerous categories of these material technologies, but one of the most prevalent material design applications is metamaterial [1], [2], [3], [4], [5], in which the coefficients of permittivity (ε) and permeability (μ) can be created negatively. As a result, it promotes material properties in communication systems more effectively than natural materials. The metamaterial can also be categorized according to a number of applications, including electromagnetic band gap (EBG) [6], [7], [8], [9], magneto dielectric [10], [11], [12], and frequency selective surface (FSS) [13], [14], [15], [16], [17], [18], [19], [20], [21], [22], [23], [24]. As a reflector in wireless communication systems, the EBG can significantly increase antenna gain. The magneto dielectric is utilized in the design of microwave frequency circuits to alter the material's coefficient to the desired value. Moreover, a FSS is a material that allows only the desired frequency to pass through and causes reflection for all other frequencies. Moreover, the FSS is continually being developed as an environmental protection material for antenna installations, as the use of conventional shielding materials causes propagation distortion. Currently, the FSS is perpetually evolving, whether as a response to a wide range of frequencies, a structure designed to be reduced in size, or a method for enhancing the antenna's gain. However, it is challenging to simultaneously accomplish multi-frequency transmission, compact dimensions, and antenna gain improvement with FSS design. Therefore, this paper presents a technique to design a multiband FSS using double layer with interdigital coplanar waveguide ICPW technique structure for use as a director to transmit multiple frequencies, with a smaller size than the conventional design and an increase in the antenna's gain when used in conjunction with an antenna, and at a low cost. The double-layer unit cell of FSS will be designed on FR-4 printed circuit board with a dielectric constant (ε_r) value of 3.2, a substrate height of 1.6 mm, a copper thickness of 0.035 mm, and a loss tangent ($\tan\delta$) of 0.04. This unit cell is capable of responding to three resonant frequencies: 1.8 GHz (LTE), 3.7 GHz (Wi-MAX), and 5.2 GHz (Wi-Fi). The front layer is composed of an ICPW structure that is based on the CPW structure [25], [26], [27], [28]. The ICPW [29], [30], [31] technique can significantly increase the capacitance between a transmission line and a lateral ground plane. It is characterized by connecting a capacitive load [32], [33], [34] to the end of the transmission line, which results in a slow wave on the transmission line and a shift of all resonant frequencies approaching zero. Due to the differences between the transmission line's electrical and physical lengths, in order to accomplish resonance at the original frequency, the transmission line's physical length must be drastically reduced, resulting in a significant reduction in transmission line size. Increasing the capacitive load affects all resonant frequencies, but it has a pronounced impact on the second-order resonance frequencies, resulting in a significant frequency shift away from zero. Since the difference in impedance within the conductor well controls the second-order resonant frequency, it is necessary to use a step-impedance [35], [36] technique on the conductor structure in conjunction with a capacitive load to achieve resonance in the desired frequency range. The back layer of the double-layer unit cell is an inverted version of the front layer, which switches between the substrate and copper to produce a square loop resonator with a double meander line. The square loop resonator [37], [38], [39] contributes to the regulation of the first-order resonant frequency in order to achieve resonance in the desired frequency range.

In addition, it facilitates the transmission of electromagnetic radiation when connected to an antenna. Capacitance occurs in the section of the double meander line [40]. This capacitance complements the capacitance of the front layer, resulting in improved slow wave properties on the front structure, thereby reducing the size of the front layer conductor from $\lambda/2$ to $\lambda/8$ compared to the conventional FSS design. In addition, it serves to regulate all resonant frequencies to accomplish resonant frequencies within the intended frequency range. The overall dimensions of the double-layer unit cell are 10.93 mm $\times$ 11.48 mm. A 7 $\times$ 7 unit cell has an overall dimension of 73.48 mm $\times$ 77.38 mm when it is connected in an array for use as an FSS director. Then, it is connected to a single-frequency dipole antenna with omnidirectional propagation and impedance matching less than -10 dB. Single-frequency dipole antennas are constructed with the same frequency as the FSS director, with gains of 1.98 dBi, 2.13 dBi, and 2.06 dBi at 1.8 GHz, 3.7 GHz, and 5.2 GHz, respectively. The simulation results indicate that electromagnetic waves are transmitted at all resonant frequencies on the FSS director when the antenna is connected to it. The antenna with the FSS director has bidirectional radiation and impedance matching at all resonance frequencies less than -10 dB. At resonant frequencies of 1.8 GHz, 3.7 GHz, and 5.2 GHz, the resonant bandwidth is 340 MHz, 810 MHz, and 2.12 GHz, respectively, and the antenna gain is 3.45 dBi, 3.05 dBi, and 3.72 dBi. Based on measurements and tests conducted on the actual work piece in the anechoic chamber room, the transmission wave of the antenna with FSS director exhibits a bidirectional propagation characteristic with an impedance matching value of less than -10 dB and bandwidths of 340 MHz, 810 MHz, and 2.12 GHz at the resonant frequencies. The antenna gain at the resonant frequencies is 3.05 dBi, 2.98 dBi, and 3.12 dBi, respectively. The design of the FSS director is described in the following section.

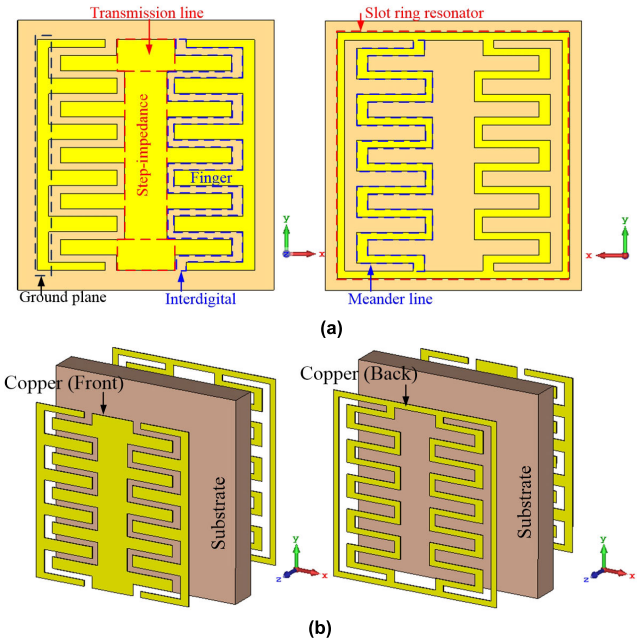

FIGURE 1. The proposed structure of FSS unit cell (a) Front and back structure of FSS unit cell (b) Material layer of FSS unit cell.

II. DESIGN OF THE DOUBLE LAYER FSS UNIT CELL

The double-layer FSS unit cell is composed of a bifacial unit cell. The front layer of the unit cell is designed with the interdigital coplanar waveguide (ICPW) technique. This technique can be used to increase the capacitance between the signal line and the side ground, as shown in the FSS unit cell structure on the left side of Fig. 1(a). The back layer depicted on the right side of Fig. 1(a) is designed with the same ICPW structure as the front structure, which is the same dimension but alternates between the layout of copper and substrate, resulting in a square loop resonator connected to a double meander line. Fig. 1(b) depicts the overall structure of the FSS unit cell. The FSS unit cell is designed for a first-order resonance frequency of 1.8 GHz (LTE) and produces second- and third-order resonance frequencies of 3.7 GHz (Wi-MAX) and 5.2 GHz (Wi-Fi), respectively. Based on the front structure, interdigital techniques can substantially enhance the capacitive value due to the presence of a finger by utilizing interdigital techniques. Along with the length and width of the finger, each finger has a space for increasing or decreasing capacitance. The capacitance generated on the FSS unit cell structure is characterized by a capacitive load connected to the end of the conductor, which shifts all resonant frequencies of the conductor to zero. The capacitance effect causes a slow-wave effect in the cable, resulting in a disparity between the cable's electrical and physical lengths. As electric length increases, the resonant frequency shifts to zero. In order to equalize both lengths and return the resonance to its original frequency, the physical length must be decreased in order to adjust the first-order resonant frequency back to the original resonant frequency. In odd mode (3, 5, 7….N) and even mode (2, 4, 7….N), however, the resonance frequencies do not resonate precisely over their original frequency range. Particularly, at the even mode frequency range, the capacitive load will cause an important shift away from zero in the original resonant frequency. If the capacitive load is substantial, it alters the second-order resonant frequency away from its initial value. The first-order resonant frequency continues to resonate at its initial frequency. The third-order resonant frequencies shift similarly to the second-order resonant frequencies, but less than the second-order resonant frequencies because the capacitive load has a significant effect on the even mode resonant frequency. Therefore, in order to regulate the strongly impacted resonance frequency, it is essential to employ a transmission line structure with step impedance [35], [36]. The transmission line impedance difference can help regulate the second-order resonant frequency. This indicates that by coupling the transmission line structure with a step impedance, the first- to third-order resonant frequencies can be controlled within the desired frequency range. Additionally, it can drastically reduce the size of the unit cell structure. However, the implementation of electromagnetic wave propagation in all three frequency bands is insufficient for transmission. Due to the characteristics of the FSS structure [13], only the first-order resonant frequency can be achieved with low-pass transmission. However, the second-order and third-order resonant frequencies are band pass transmissions, but they cannot transmit effectively. In order for the second-order and third-order resonance frequencies to transmit well and to avoid distorted resonance, the capacitive load must be increased by creating an inverted layout of the front unit cell to the back layer using copper and substrate of the same size. By alternating between a copper and substrate layout, the back layer is comprised of a square loop resonator [37] coupled to a double meander line [40]. The square loop resonator produces the first-order resonance frequencies as same as the front structure, while the meander line contributes to the second-and third-order resonance frequencies. As shown in Fig. 2(a), a significant capacitive effect was observed on the structure when analyzing the front and rear of the unit cell. It can be seen that capacitance C_i will exist between the transmission line and ground on the front structure when the ICPW technique is used. Due to the interdigital technique, the capacitance C_i will occur primarily on the structure. The capacitive increase in those areas of the structure will be affected by the finger's width, length, and number. For C_i'/2, it represents the capacitance between the transmission line and ground within the substrate. Due to the electrical coupling of the ground to the square loop resonator and the transmission line to the square loop resonator, the capacitance C_g will develop within the substrate. Moreover, capacitance C_g is greater than capacitance C_i'. In addition, it was discovered that the coupling effect between the ground and the square loop resonator resulted in a capacitance C_f with minimal influence on the resonance. In the final part, C_c represents the capacitance of the meandering line. It influences the second-and third-order resonant frequencies, which

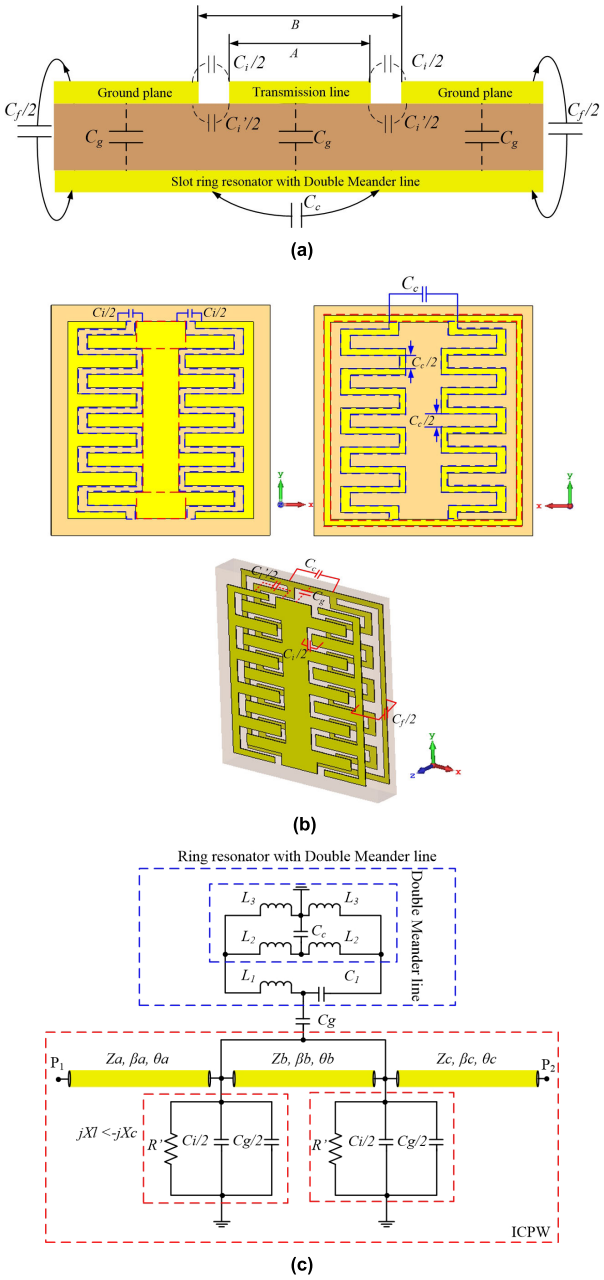

FIGURE 2. The proposed unit cell and parameters of the equivalent circuit in (a) cross section of unit cell, (b) 2d and 3d dimension, (c) transmission line section.

are used to complement the C_i and C_g values of the front-side FSS structure that controls the frequency resonance in this range. When A represents the transmission line width and B represents the transmission line width to ground, the capacitive effect on each structure can be classified as depicted in Fig. 2(b). It is discovered that C_g and C_f are connected to the anterior and posterior structures. Consequently, these two components are related to the frequency range resonance, which is depicted in Fig. 2(c) as an equivalent circuit. The ICPW segment of the transmission line is composed of the internal impedance of Z, the propagation constant of β, and the electrical length of θ. In the event that the transmission line has the same impedance, the total impedance (Z_t) equals $Z_t = Z_a = Z_b = Z_c$, the propagation constant (β_t) represents $\beta_t = \beta_a = \beta_b = \beta_c$, and the total electrical length (θ_t) is $\theta_t = \theta_a = \theta_b = \theta_c$. When step-impedance techniques are applied to the transmission line, the total impedance is $Z_t = Z_a + Z_b + Z_c$, the propagation constant has become $\beta_t = \beta_a + \beta_b + \beta_c$, and the total electrical length represents $\theta_t = \theta_a + \theta_b + \theta_c$. There is a capacitance connection between the transmission line and the ground in each phase. It has been discovered that the capacitance of C_i in the interdigital phase has the reactance $jX_L < -jX_c$, where R' is the transmission line loss. In addition, C_g is produced by the electrical coupling between the ground and the back framework, which increases capacitance in the interdigital region. Since the connection between C_g and C_i is parallel, the capacitance connected to the transmission line will have the characteristics of a connection at the transmission line's end. For the dorsal structure of a unit cell with a square loop resonator and a double meander line structure, it has been determined that the square loop resonator consists of an equivalent circuit of inductor L_1 and capacitive C_1 connected to the double meander line structure. Each segment's length on the meander line corresponds to the inductive values L_2 and L_3. Additionally, the capacitance C_c is formed within this double meander line structure. According to connecting the front and rear FSS unit cell structures, the electrical coupling between the transmission line of the front layer and the square loop resonator structure generates the capacitance C_g, which is identical to the capacitance C_g generated between the ground of the front layer and square loop resonator. Consequently, the capacitive load connected to the conductive end of the ICPW structure is increased due to the sum of the capacitances $C_i + C_g + C_c$, resulting in a greater resonant effect caused by the slow wave on the transmission line than with conventional transmission line structures. The total capacitance of the C_{ICPW} structure is represented by (1) [13], [28].

$$C_{ICPW} = C_i + C_i' + C_g + C_f + C_c \tag{1}$$

When

$$C_i = \frac{(\varepsilon_r + 1)}{L_t} L_f (\varepsilon_r + 1)(0.1(n-3) + 0.11)$$

$$C_i' = \frac{\varepsilon_0 \varepsilon_r}{\pi} \ln\left[\cot h\left(\frac{\pi}{4}\frac{B}{h}\right)\right] + 0.65\, c_f \left(\frac{0.02}{B/h} + 1 - \frac{1}{\varepsilon_0^2}\right)$$

$$C_g = \varepsilon_0 \varepsilon_r \frac{A}{h}$$

$$C_f = \frac{\sqrt{\varepsilon_r}}{(C_i) - (C_g)}$$

$$C_c = 3.937 \times 10^{-5} l (\varepsilon_r + 1)(0.11(N-3) + 0.252)$$

L_t represents the entire length of the interdigital segments connected to the transmission line in (1). L_f depicts the finger length, n indicates the number of fingers, h is the substrate height, N represents the number of turns of the meander line, and l is the entire length of the meander line. For the

FSS unit cell utilizing the square loop resonator and double meander line technique, the inductive and capacitive values of the square loop resonator structure can be calculated using (2) [37]. Also, w is square loop width, d is square loop length, p is periodicity of the strip, g is the inner-loop gap, θ is angle of incidence, G(p, w, λ, θ) is correction factor for the associate inductance and G(p, g, λ, θ) is correction factor for the associate capacitance.

$$\frac{\omega L_1}{Z_0} = \frac{d}{p}\cos\theta \times F\left(p, w, \lambda, \theta\right)$$
$$\frac{\omega C_1}{Y_0} = 4\frac{d}{\lambda}\sec\theta \times F\left(p, g, \lambda, \theta\right)\varepsilon_{eff} \quad (2)$$

when

$$F\left(p, w, \lambda, \theta\right) = \frac{p}{\lambda}\left[\ln\cos ec\left(\frac{\pi w}{2p}\right) + G\left(p, w, \lambda, \theta\right)\right]$$
$$F\left(p, g, \lambda, \theta\right) = \frac{p}{\lambda}\left[\ln\cos ec\left(\frac{\pi g}{2p}\right) + G\left(p, g, \lambda, \theta\right)\right]$$

The square loop resonator's first order resonance frequency can be calculated using the (3), in which L_r is the circumferential length of the loop, N_r is the mode number, f_0 is the first order resonance frequency, and C is the speed of light.

$$L_r = N_r\lambda_g \quad (3)$$

When

$$\lambda_g = \frac{C}{f_0\sqrt{\varepsilon_{eff}}}$$

According to equation (3), the width and length of the double meander line on the left and right sides are identical. L_2 and L_3 can be calculated using equation (4) [40], where Z_c is the meander line's characteristic impedance, ε_{eff} is the effective dielectric constant, and w is the meander line's width.

$$L_2 = L_3 = \left(\frac{Z_c\sqrt{\varepsilon_{re}}}{C}\right)/2\left(\frac{Z_c\sqrt{\varepsilon_{re}}}{C}\right) \quad (4)$$

In the case that the conductors in the ICPW section have the same impedance $Z_a = Z_b = Z_c$, the total impedance can be calculated using (5), where K is the complete elliptic integral of the first kind [28].

$$Z_t = \frac{60\pi}{\sqrt{\varepsilon_{eff}}}\frac{1}{\left(K\left(k\right)/K\left(k'\right)\right) + \left(K\left(k_x\right)/K\left(k'_x\right)\right)} \quad (5)$$

When

$$\varepsilon_{eff} = \left[1.0 + \frac{K\left(k'\right)}{K(k)}\frac{K\left(k_x\right)}{K\left(k'_x\right)}/1.0 + \frac{K\left(k'\right)}{K(k)}\frac{K\left(k'_x\right)}{K\left(k_x\right)}\right]$$
$$k = \frac{A}{B}, k' = \sqrt{1.0 - k^2}$$
$$k_x = \tanh\left(\frac{\pi A}{2h}\right)/\tanh\left(\frac{\pi B}{2}h\right), k'_x = \sqrt{1.0 - k_x^2}$$
$$\beta_t = \frac{2\pi}{\lambda}$$

In the event that step-impedance techniques are applied to the transmission line, the impedance value $Z_a = Z_c$, which is the ratio with Z_b, will determine the ratio R_z, where $R_z = (Z_a/Z_b) = (Z_c/Z_b)$. The transmission line's impedance can be calculated using (6) [35], [36].

$$Y_t = \frac{1}{Z_t} = jY_b\frac{2\left(1 + R_z\right)\left(R_z - \tan^2\theta_t\right)\tan\theta_t}{k - 2\left(1 + R_z + R_z^2\right)\tan^2\theta_t + R_z\tan^4\theta_t} \quad (6)$$

From (1)-(6), it can be determined that the capacitance of the double FSS unit cell's anterior and posterior structures are related. The ICPW structure receives capacitance from the double meander line to supplement the capacitive load connected to the structure's transmission line. Therefore, it can be explained that the first- to third-order electrical length and the resonant frequency are affected by the capacitive load according to (7) [22], [28], [29], [30]. As assigned θ_{a0}, θ_{a1} and θ_{a2} represent the electrical length at the first-, second-, and third-order resonant frequencies, respectively. Also, the f_0, f_1, and f_2 are the resonant frequencies of the first-, second-, and third-order.

$$\theta_{a0} = 2\tan^{-1}\left(\frac{1}{\pi f_0 Z_t\left(C_i + C_g + C_c\right)}\right)$$
$$\theta_{a1} = 2\pi - 2\tan^{-1}\left(\pi f_1 Z_t\left(C_i + C_g + C_c\right)\right)$$
$$\theta_{a2} = 2\tan^{-1}\left(\frac{1}{\pi f_2 Z_t\left(C_i + C_g + C_c\right)}\right) \quad (7)$$

It can be seen from (7) that the capacitive load (C_i, C_g, C_c) connected to the transmission line affects all resonant frequencies, but has a pronounced influence on the second order or even mode (2, 4, 6, 8....) of the resonant frequency. In addition, Z_t has a major influence. This implies that the method for controlling the first-order resonant frequency is dependent on the dimensions of the transmission line and square loop resonator. The connected capacitive will cause all resonant frequencies to move closer to zero, thereby reducing the cable's physical length and shifting the first resonant frequencies back to their original frequency. Since the electrical and physical lengths are not identical, the transmission line is affected by the slow wave effect. However, the second-order

TABLE 1. Parameters of double layer FSS unit cell.

Substrate (mm)	Front (mm)	Back (mm)
L_1 = 11.48	L_3 = 2.91	L_{14} = 10.48
	L_4 = 9.83	L_{15} = 9.93
	W_5 = 0.50	W_{16} = 0.48
	W_6 = 0.35	W_{17} = 0.49
	W_7 = 0.67	W_{18} = 0.67
	L_8 = 2.50	L_{19} = 2.89
L_2 = 10.93	L_9 = 3.42	W_{20} = 0.33
	W_{10} = 1.31	L_{21} = 3.24
	L_{11} = 1.80	W_{22} = 0.33
	W_{12} = 0.65	W_{23} = 1.31
	L_{13} = 7.30	W_{24} = 0.33
	h=1.6	W_{25} = 0.33

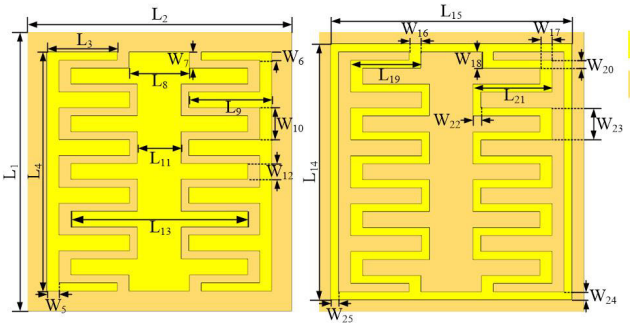

FIGURE 3. The proposed unit cell configuration and parameters.

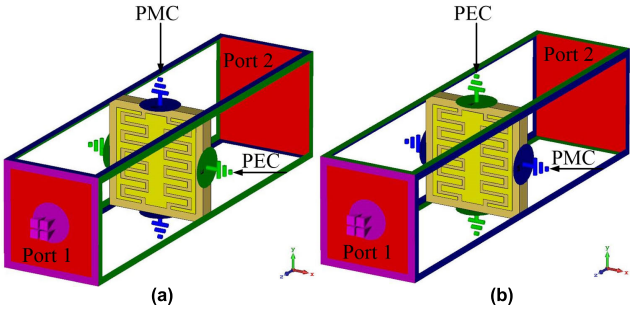

FIGURE 4. The wave transmission test in (a) first case and (b) second case.

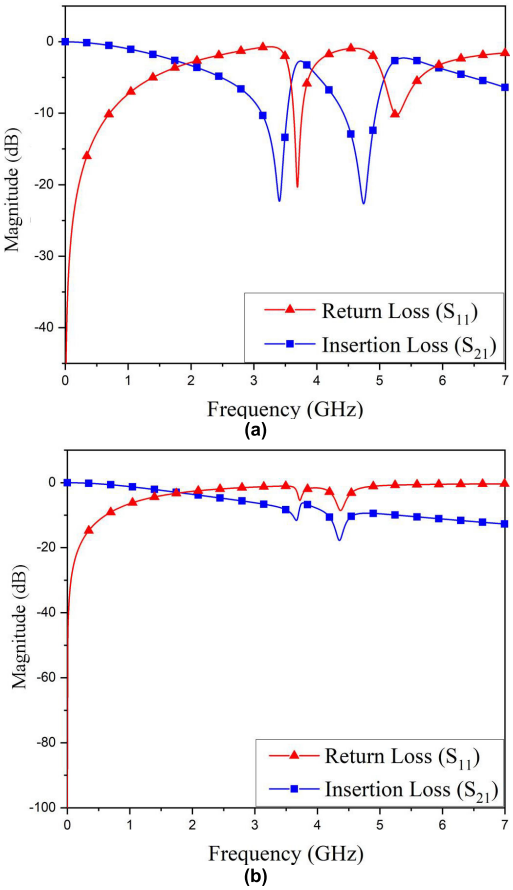

FIGURE 5. The simulation result of S_{11} and S_{21} with (a) PMC on Y-axis and PEC on X-axis and (b) PEC on Y-axis and PMC on X-axis.

and third- order resonance frequencies cannot achieve resonance at the original frequency range, so the capacitive value must be controlled by adjusting the finger size along with the meander line structure and utilizing step-impedance techniques on the transmission line to achieve the desired resonance frequency. For third-order resonant frequencies, the capacitive loads generated by the front and rear structures are applied in accordance with the intended resonant frequency band. According to the design, the dimension of the unit cell structure was decreased from $\lambda/2$ to $\lambda/8$, and the desired response of three resonance frequencies was achieved. Fig. 3 and Table 1 illustrate the structure and parameters of the double-layer FSS unit cell.

From the double layer FSS unit cell design, it is evaluated the wave transmission along the operating frequency by utilizing the CST program. The simulation configuration is shown in Fig. 4. a transmittance test was divided into two cases, with the first case assigned the X-axis as E-field (PEC), and the Y-axis as H-field (PMC), as shown in Fig. 4(a) and the second case sets the X-axis as H-field (PMC) and the Y-axis as E-field (PEC), as shown in Fig. 4(b). The configuration described above will test the transmission of electromagnetic waves through the FSS unit cell structure, where the axis designated as the E-field will be the path of the current from the excitation source causing the resonance frequency of the structure, and it will be aligned with the antenna that will be used in conjunction with the transmission of electromagnetic waves. This causes port 1 to transmit waves to port 2 via the FSS unit cell. To determine the transmission coefficient (S_{21}) and reflection coefficient (S_{11}), each port is situated at a distance of $\lambda/2$ at the first-order resonant frequency. With PEC along the X-axis and PMC along the Y-axis, wave transmission can be attained at the specified resonant frequency ranges of 1.8 GHz, 3.7 GHz, and 5.2 GHz, according to the configurations described above. The simulation result of the S_{11} and S_{21} are shown in Fig. 5(a). It can be seen that the insert loss (S_{21}) represents low-passed at the first-order resonant frequencies, while it indicates band-passed at the second-and third-order resonant frequencies. The frequency response of the wave transmission from port 2 to port 1 will be identical. Fig. 5(b) depicts the simulation result of S_{11} and S_{21} for PEC along the Y-axis and PMC along the X-axis. It has been found that the electromagnetic wave can only transmit at one of the first-order resonant frequencies, but not at the second- and third-order resonant frequencies. Using simulations to evaluate the transmittance, it was determined that the transmission was most effective when the PEC was aligned with the interdigital arrangement along the X-axis. The resonance frequency response is satisfactory. The simulation findings are depicted in Fig. 5. Fig. 6(a) clearly demonstrates that transmission is satisfactory in the intended resonance frequency range. Observing the resultant phase

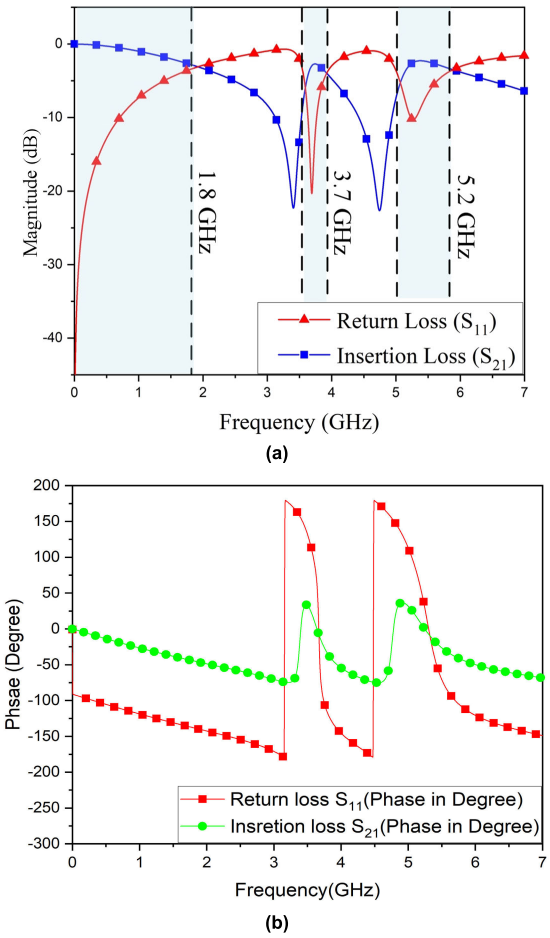

FIGURE 6. The simulation result of proposed FSS unit cell (a) Magnitude of S_{11} and S_{21} and (b) Phase of S_{11} and S_{21}.

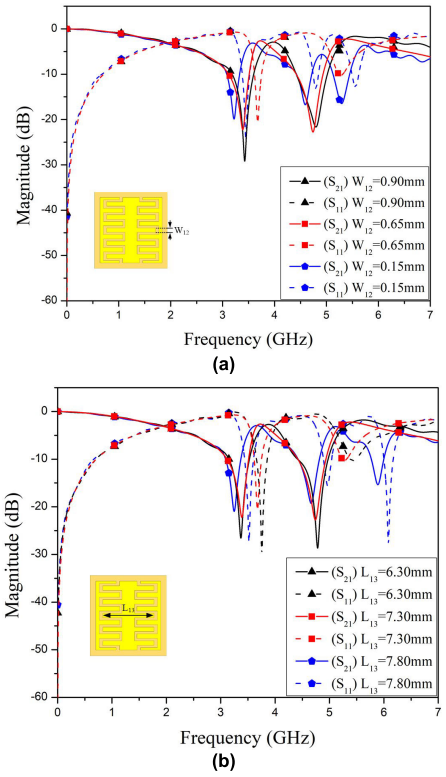

FIGURE 7. The simulation result of $|S_{11}|$ and $|S_{21}|$ with adjustment of the transmission line structure's parameters (a) W_{12} and (b) L_{13}.

effect in Fig. 6(b), it is discovered that there is a change in phase polarity at the second- and third-order resonance frequency ranges with bandpass characteristics corresponding to the transmission and reflection coefficients in Fig. 6(a). It verifies that the second and third-order resonant frequencies can be controlled within the desired frequency range due to the technique implemented within the FSS unit cell structure. At first-order resonant frequencies, the magnitude of $|S_{21}|$ is the low pass but there is no change in phase polarity; thus, it depends on the characteristics of the conduction structure at the first-order resonance frequency. By increasing the capacitive load values of the ICPW and mender line, the significant unit cell structure parameters are evaluated. There is evidence that second- and third-order resonance frequencies have shifted significantly. Fig. 7 depicts the adjustment of the transmission line structure's parameters. It has been discovered that adjusting the finger parameters of W_{12} and L_{13} in the interdigital phase decreases or increases the capacitive (C_i) value of the structure. Clearly, this capacitive value impacts the shift at all resonant frequencies, but it has a particularly large effect on the shift at the second-order resonance frequencies. Depending on the extent of the finger's width and length, the resonant frequency increases or decreases, resulting in a change in capacitance. As stated previously, the capacitance will affect the resonant frequency. Adjusting the parameters of the double meander line's width W_{22} and length W_{23} altered the capacitive value (C_c). This capacitance has an impact on all resonant frequencies. Particularly, it will result in a significant change in resonance at second-order resonant frequencies, as shown in Fig. 8. The capacitance generated on the anterior and posterior structures of the FSS unit cell has a significant impact on the resonance frequency, particularly the second-order resonance frequency, as shown in Figs. 7 and 8. The capacitive part of the double meander line enhances the capacitive value of the ICPW structure, drastically reducing the size of the FSS unit cell as a result of the large slow waves on the transmission line corresponding to the capacitive value and controlling the desired resonant frequency range. Fig. 9 displays the simulation results of $|S_{11}|$ and $|S_{21}|$ as the number of fingers increases. It has been discovered that the resonant frequency decreases. Since the number of fingers directly affects the capacitive increase or decrease, causing a substantial shift in the resonant frequency, the number of fingers must be appropriate for increasing the capacitive value in order to control the resonant frequency. By adjusting the parameters as depicted in Figs. 7-9, it is discovered that it affects all resonance frequencies, but has a strong effect on second-order or even-mode resonance frequencies and a moderate effect

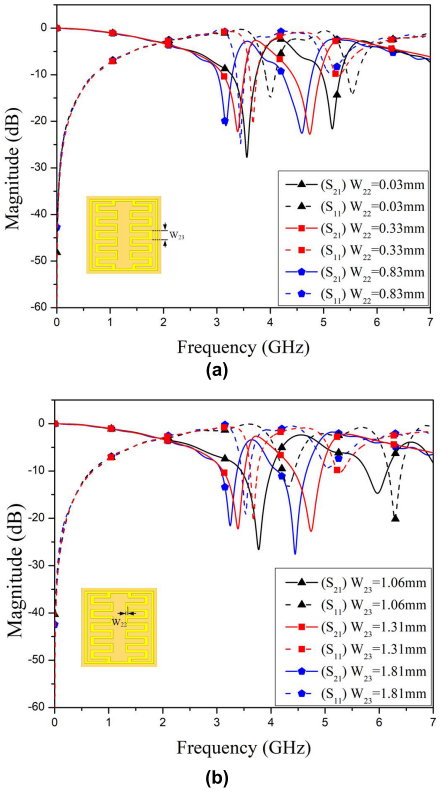

FIGURE 8. The simulation result of $|S_{11}|$ and $|S_{21}|$ with adjustment of the double meander line parameters (a) W_{23} and (b) W_{22}.

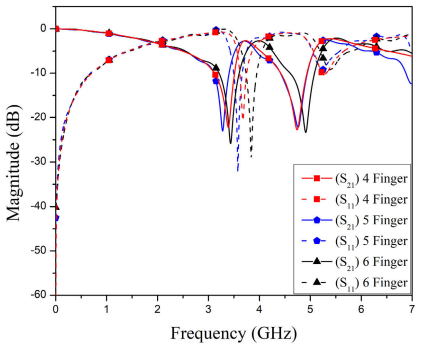

FIGURE 9. The simulation result of $|S_{11}|$ and $|S_{21}|$ with increasing the finger number.

on first-order and third-order resonance frequencies or odd mode, as determined by the design equation. In the process of adjusting the step-impedance parameters L_8 and L_{11}. As shown in Fig. 10, the difference in impedance within the transmission line influences the control of the second-order resonant frequency, but not the first- and third-order resonant frequencies. That corresponds to the design equation. Fig. 11 depicts the simulation results of the E- and H- field on the FSS unit cell structure, illustrating its effects on the front- and rear-structure of the proposed unit cell. By exciting the E-field along the X-axis and the H-field along the Y-axis as depicted in Fig. 11(a), it is possible to evaluate the

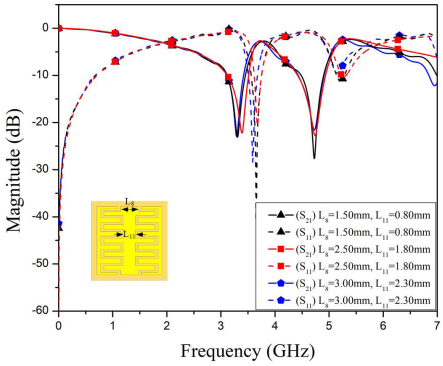

FIGURE 10. The simulation result of $|S_{11}|$ and $|S_{21}|$ with adjusting the step-impedance parameters L_8 and L_{11}.

effect of the E- and H-fields on the front structure, which consists of the transmission line applied with ICPW and step impedance techniques. At the first-order resonant frequency, the E-field is most prevalent in the interdigital portion of the transmission line structure. It indicates that the interdigital portion of the transmission line structure is responsible for generating this resonant frequency. There is a large quantity of E-field in the interdigital range and a small amount on the transmission line for second-order resonant frequencies because, at this resonant frequency, it is primarily controlled by the capacitance generated by the interdigital component and a step impedance component of the transmission line. Therefore, these components can facilitate the regulation of second resonant frequencies. For third-order resonance frequencies, a certain amount of E-field values are formed on the interdigital structure. It can be described that the ICPW Structure of the FSS unit cell can control this resonant frequency due to the capacitance created by the structure. It is evident that the interdigital structure responds effectively to the E-field. After simulating the operation with the E-field along the Y-axis and the H-field along the X-axis, as shown in Fig. 11(a), It was discovered that the H-field response in the ICPW configuration was insignificant in relation to the E-field across all resonant frequencies. Fig. 11(b) demonstrates the simulation result of exciting the E- and H-field on the square loop resonator structure with a double meander line, with the E-field along the X-axis and the H-field along the Y-axis. According to Fig. 11(b), the E-field is most prevalent on the square loop resonator structure at the first resonant frequency. It appears the square loop resonator influences this frequency. Due to the capacitance of the structure's effect on the second resonant frequency, the double meander line exhibits the greatest E-field. At the third resonant frequency, the E-field appears substantially on the structure of the square loop resonator and double meander line. The third resonant frequency is governed by a combination of the square loop resonator and the double meander line. Then, the E-field and H-field will be reassigned along the Y- and X-axes respectively to observe the field effects at each resonant frequency.

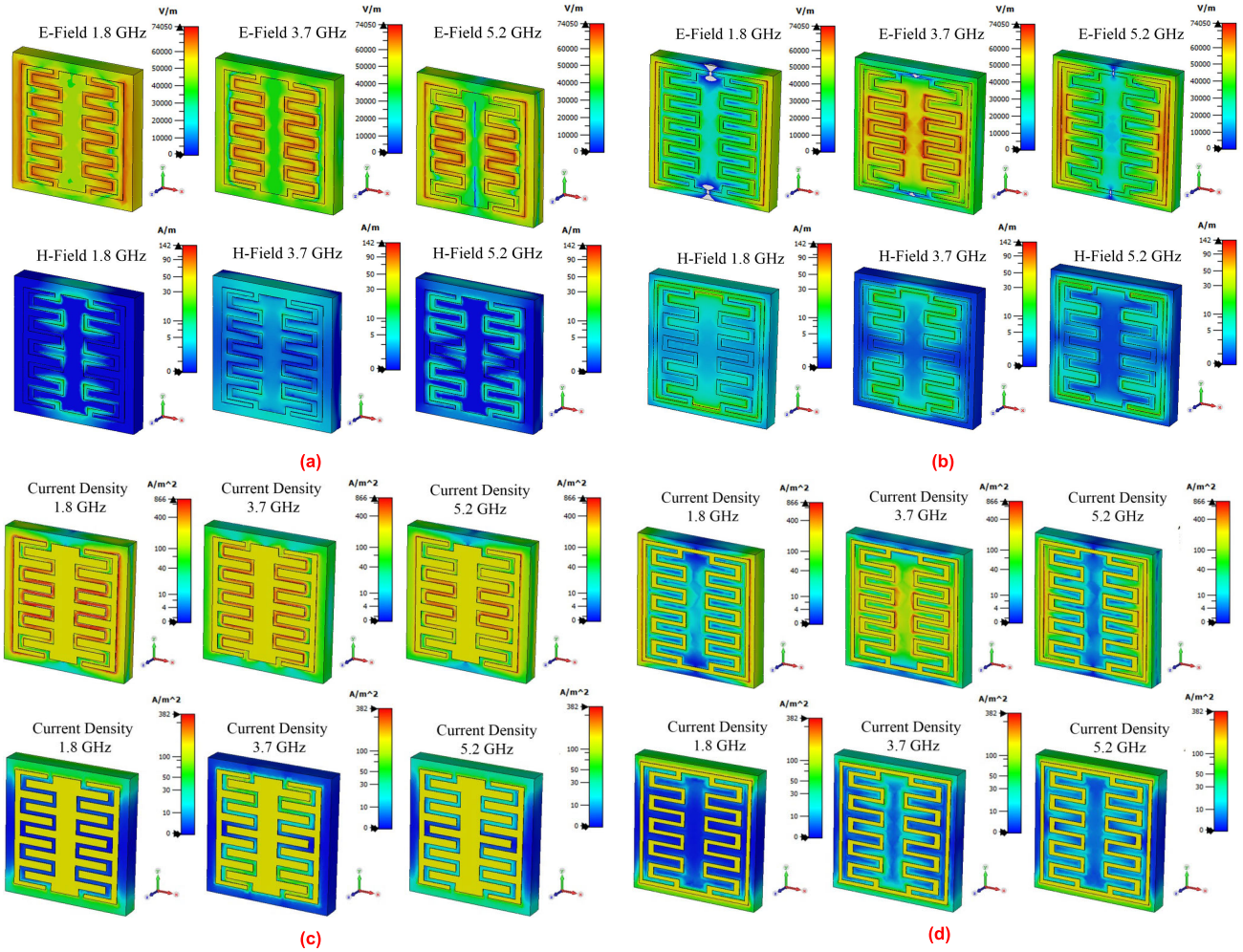

FIGURE 11. The simulation results on the proposed unit cell of (a) the E-filed and H-field at front layer, (b) the E-field and H-field at back layer, (c) current distribution with Ex-Hy and Ey-Hx at front layer, and (d) current distribution with Ex-Hy and Ey-Hx at back layer.

However, the square loop resonator and double meander line do not response the H-fields in the X-axis direction.

Fig. 11(c) depicts the current distribution observed at the front layer when the electric field is oriented along the X-axis and the magnetic field is oriented along the Y-axis. The findings indicate that the suggested unit cell exhibits a substantial current density, as evidenced by the E-field and H-field evaluations along the X-axis and Y-axis, respectively, as depicted in Figure 11(a). In contrast, the electric field and magnetic field are oriented along the Y-axis and X-axis, respectively. According to the outcome of the E-field along the Y-axis and H-field along the X-axis in Fig. 11(a), it is suggested that the current distribution possesses a clearly reduced state in the unit cell. Fig. 11(d) illustrated the current distribution observed at the back layer. The electric and magnetic fields are oriented along the X and Y-axes. The analysis of the E-field and H-field along the X-axis and Y-axis, respectively, as illustrated in Figure 11(b), indicates a significant concentration of the current distribution within the unit cell. In contrast, when the electric and magnetic fields are oriented along the Y and X-axes, respectively. Based on the E-field and H-field assessments along the Y-axis and X-axis, respectively, as illustrated in Figure 11(b), it can be revealed that the current distribution within the unit cell is significantly low. According to the simulation results of E-field and H-field on the FSS unit cell as shown in Figs. 11, the structure of ICPW and square loop resonator with double meander line responds well to E-field along the X-axis. Therefore, the location of the dipole antenna to be evaluated with the FSS unit cell must have the direction of the current along the X-axis. In addition, it was found that the E-field responses on the anterior and posterior structures were consistent with the controlled resonant frequency characteristics and design equations. Fig. 12 illustrates the comparison of properties between the proposed FSS unit cell and a conventional CPW unit cell. Fig. 12(a) depicts a dimension comparison between the proposed FSS unit cell and a typical CPW unit cell of $\lambda/2$. Both unit cells were designed at the same initial resonant frequency of 1.8 GHz. As the simulation result of the frequency response depicted in Fig. 12(b), both structures generate identical first-order resonance frequencies, whereas conventional CPW unit cell structures are incapable of pro-

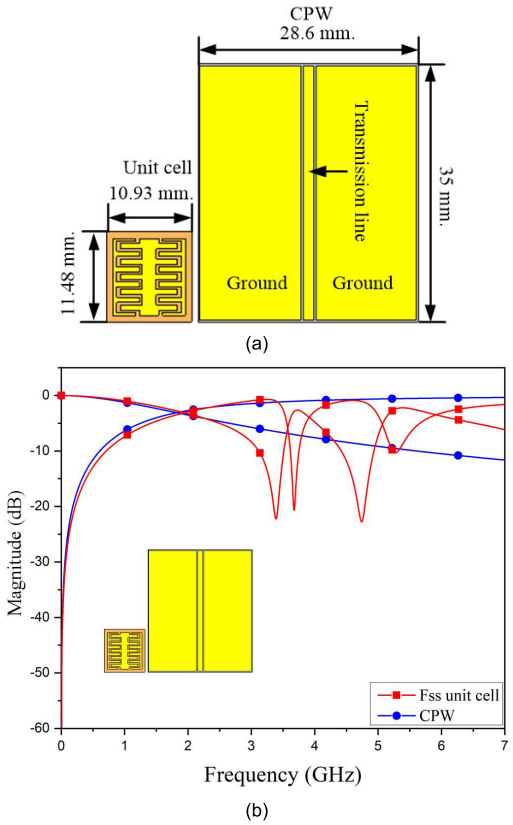

FIGURE 12. Comparison of properties between the proposed unit cell and typical unit cell (a) dimension and (b) frequency response of |S11| and |S21|.

TABLE 2. Dipole antenna dimension.

Dipole parameters	Dimension (mm)		
	f = 1.8 GHz	f = 3.7 GHz	f = 5.2 GHz
L_S	32.50	14.5	10.5
L_T	68.00	46.0	22.0
G	3.00	2.2	1.00
A	3.46	3.46	3.46
T	0.46	0.46	0.46

ducing the second and third resonant frequencies. In addition, the dimension of the proposed FSS unit cell is much smaller than that of a typical unit cell. In the next section, the FSS unit cell is arrayed and connected to a single-frequency dipole antenna in order to evaluate its transmittance characteristics in the resonant frequency range.

III. DESIGN OF THE ARRAY DOUBLE LAYER FSS UNIT CELL CONNECT WITH DIPOLE ANTENNA

In this section, the double FSS unit cell is arrayed to form an FSS director structure. As this is the optimal size for evaluating the FSS director in conjunction with a dipole

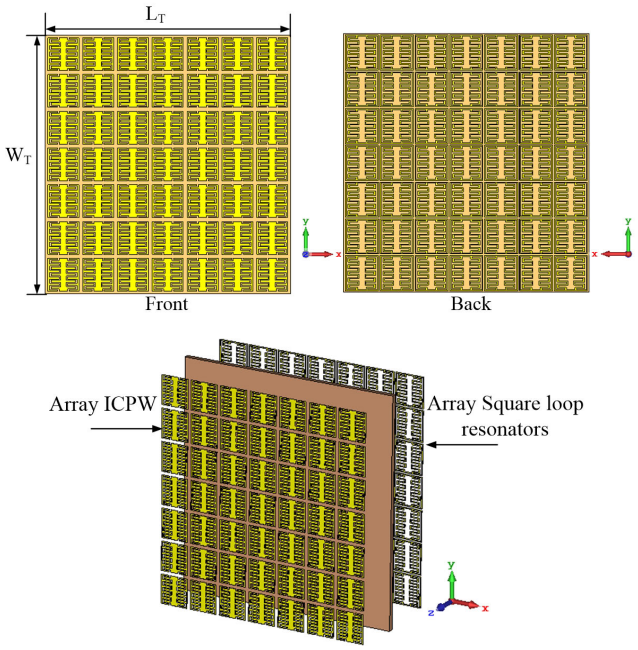

FIGURE 13. The proposed FSS director configuration illustrates of front, back, and side views.

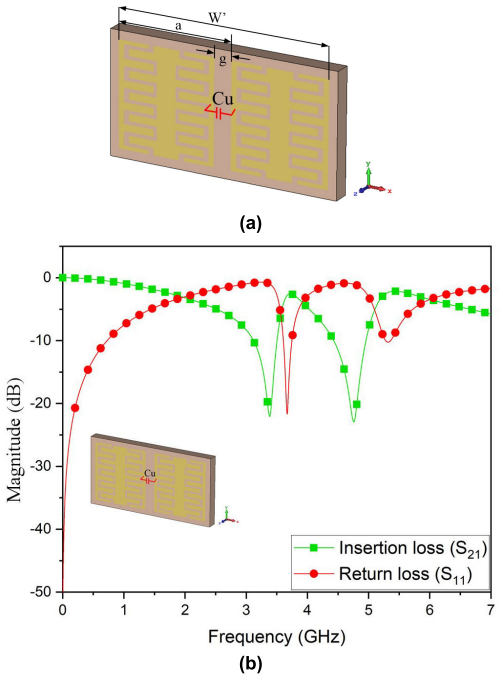

FIGURE 14. The connection between the proposed unit cell (a) configuration (b) simulation result of the $|S_{11}|$ and $|S_{21}|$.

antenna, there will be a number of 7 × 7 unit cells. Fig. 13 depicts the proposed director that was derived from the FSS unit cell arrangement. It reveals that the front and back layers of ICPW and square loop resonator have been reorganized. The FSS director's total length and width are 73.48 mm and 77.38 mm, respectively. By electrically coupling FSS unit cells, the capacitive coupling will occur between each unit cell structure's gap. If the capacitance coupling is substantial,

TABLE 3. Comparison of the proposed multiband FSS with antenna in references.

Reference Number	No. of bands (structure shaped)	Freq.(GHz)	Unit cell size (mm^3)	Overall size (mm^3)	No. of unit cell array	Measurement gain (dB), beam direction (degree)	Type of Applications
[13]	3 (Square patch combine element)	4.66, 9.6 and 20	19×19×2.2	23.6×23.6×2.2	2×2	-	Fss Transmission
[14]	1(square patch)	3.2-12	15.75×15.75×2.2	30×60×1.6	13×5	3-4, (0°)	FSS Reflector
[15]	3 (Transmission line patch)	10.5,14 and 19	9.5×6×1.524	38×24×1.524	4×1 (4 layer)	-	Fss Transmission
[16]	1 (Open Matryoshka Element)	1.0-1.8	24×24×0.97	240×240×0.97	10×10	-	Fss Transmission
[17]	1(GDSL)	1.0-12, 12-18 and 18-26	5×5×1	15×15×1	3×3	-	Fss Transmission
[18]	2 (Circular loop)	2.4, 5.8	25.6×1.7×1.6	25.6×1.7×1.6	1	-	FSS Control frequency
[19]	3 (Multi layer PIN Diode FSS)	1.2, 2.6 and 4.1	20×20×1	20×20×1	1	-	FSS Transmission
[20]	1 (MUC FSS)	28-31	3.4×5.6×0.508	13×9×0.508	3×5	11, (34°) 11, (28°) 10.4, (25°)	FSS Reflector
[21]	1 (Square patch)	4-6 and 7-9	6×6×0.1	100×100×0.1	6×14	9.5, (0°)	FSS Reflector
[22]	3 (Aperture Interdigital)	1.8 3.7 5.2	11.53×10.77×1.6	86.16×92.32×1.6	8×8	3.67, (7°) 3.16, (10°) 3.42, (2°)	FSS Director
[23]	1 (2 layer cDRAs.)	5.2,5.5 and 5.8	15.75×15.75×2.2	126×126×2.2	6×8	More 12, (±45°)	FSS Reflector
FSS proposed	3 (ICPW with Meander line)	1.8 3.7 5.2	10.92×11.48×1.6	73.48×77.38×1.6	7×7	3.03, (0°) 2.98, (0°) 3.12, (0°)	FSS Director

the resonant frequency spectrum will be altered. To achieve a unit cell spacing devoid of electrical coupling, it is necessary to maintain a distance between the metal margins equal to 0.7 times the substrate height (h), as this is the shortest distance at which the electromagnetic field has no effect on the structure. As a consequence of the assembly of the proposed unit cell to the array, the capacitance of C_u during the proposed unit cell will be occurred, as depicted in Fig. 14. During simulations, it was discovered that the connection between the FSS unit cells had no impact on the resonance at the intended frequency range. This indicates that the electrical coupling between structures is so minimal that it has no effect on resonance. The capacitance produced during coupling and affecting the resonant frequency can be calculated using (8).

$$\theta_{a0} = 2\tan^{-1}\left(\frac{1}{\pi f_0 Z_t \left(C_i + C_g + C_c + C_u\right)}\right)$$

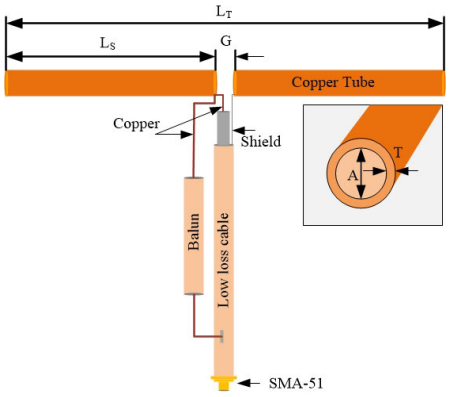

FIGURE 15. The dipole antenna configuration created by copper tube connected to balun and fed by SMA-51.

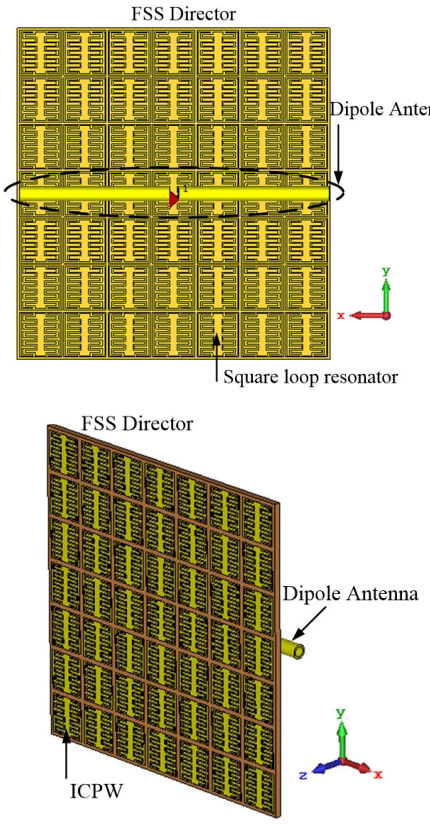

FIGURE 16. The proposed structure of dipole antenna with FSS director (a) 2D view (b) 3D view.

$$\theta_{a1} = 2\pi - 2\tan^{-1}\left(\pi f_1 Z_t \left(C_i + C_g + C_c + C_u\right)\right)$$
$$\theta_{a2} = 2\tan^{-1}\left(\frac{1}{\pi f_2 Z_t \left(C_i + C_g + C_c + C_u\right)}\right) \quad (8)$$

When

$$C_u = \frac{W'\varepsilon_0(1+\varepsilon_r)}{\pi}\cosh^{-1}\left(\frac{a}{g}\right)$$

Let a is the length of unit cell including gap, g is the gap between each unit cell, and W' is the width of the array

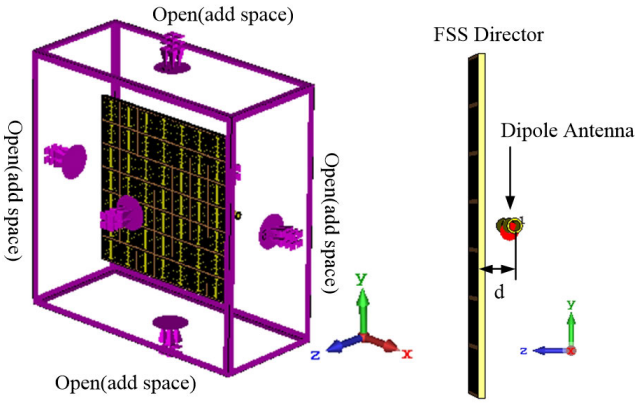

FIGURE 17. The boundary condition configuration of the simulation process for the antenna with the FSS director.

FSS unit cell structure, as illustrated in Fig. 14(a). Equation (8) demonstrates that the coupling capacitance value of C_u created during the unit cell connection influences all resonant frequencies, particularly the second resonant frequency. For resonant frequency accuracy, the C_u value must be calculated and incorporated into the capacitance value delivered by the unit cell structure for each FSS unit cell structure with a distance less than 0.70 times the substrate height (h). The C_u value of the proposed FSS unit cell structure has no effect on the resonant frequencies. After observing the characteristic of the array FSS unit cell arrangement, it will be combined with a single frequency dipole antenna that radiates the omnidirectional pattern. Copper material is used to produce a typical single-frequency dipole with resonant frequencies of 1.8 GHz, 3.7 GHz, and 5.2 GHz and antenna gains of 1.97 dBi, 2.12 dBi, and 2.05 dBi, respectively. Fig. 15 illustrates the dipole antenna configuration produced by a copper tube with compensating current utilizing the balun technique. In addition, the dipole antenna is fed by an SMA-51 connector. The dipole antenna parameter at each resonance frequency is shown in Table 2. Let L_s represent the length of each copper tube, L_t is the total length of the copper tube, G defines the gap of the dipole antenna, A indicates the diameter of the copper tube, and T is the thickness of the copper tube. The combination of the dipole antenna and the FSS director is depicted in Fig. 16. According to Fig. 16, the dipole antenna will be positioned along the X-axis because the E-field of the FSS unit cell, which previously simulated wave propagation, responds favorably in the direction of the X-axis. As a consequence, the antenna's current flows in the same direction as the E-field, resulting in an enhancement of the electromagnetic wave at the resonant frequency. In addition, the antenna will be positioned behind the FSS director in order to transmit electromagnetic wave from behind to the front director. A single-frequency dipole antenna will be used in conjunction with the FSS director at each of its resonant frequencies to simulate the operation of an FSS director's performance. Because the multiband or wideband

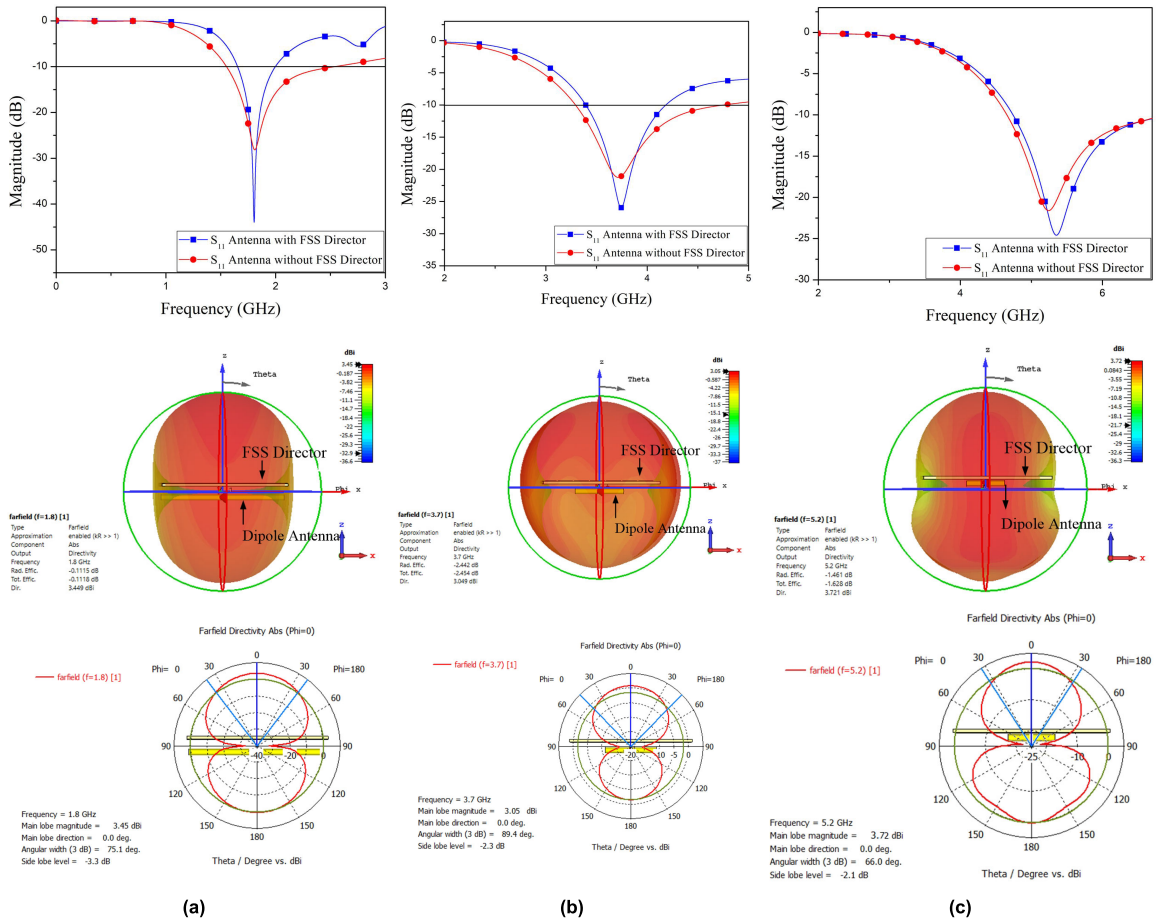

FIGURE 18. The simulation results of frequency response, radiation pattern with gain at the frequency of (a) 1.8 GHz, (b) 3.7 GHz, and (c) 5.2 GHz.

antenna with the FSS director will have a significant loss at high frequencies, demonstrating the FSS director's optimal performance is unfeasible. Fig. 17 illustrates the simulation process.

The boundary condition of the simulation process for the antenna with the FSS director will be established to the open add space, simulating the workpiece placement environment as a free space environment. The distance between the antenna and the FSS director is dependent on the unit cell size of the FSS. Since an antenna with a director or reflector of approximately $\lambda/2$ is typically positioned at a distance of approximately $\lambda/4$, this distance is suitable for enhancing the phase of the antenna. Nonetheless, if the size of the unit cell structure is less than $\lambda/2$, the spacing between the antenna and the FSS director will be less than $\lambda/4$, depending on the resonant frequency range applied. The distance between the antenna and the proposed FSS director will be a parameter of d. At the resonant frequency of 1.8 GHz, 3.7 GHz, and 5.2 GHz, the distance of d is 15.70mm, 11.24 mm, and 8.46 mm, respectively. Figs. 18(a) through 18(c) depict the simulation results of the antenna with and without FSS director at 1.8 GHz, 3.7 GHz, and 5.2 GHz, respectively. At 1.8 GHz, it has been determined that the antenna with FSS director has an impedance bandwidth of 340 MHz (1.65GHz-1.99 GHz) with $|S_{11}| < -10$ dB and a bidirectional radiation pattern with a gain of 3.45 dBi at 0 degrees, as shown in Fig. 18(a).

Fig. 18(b) illustrates the characteristic of the antenna with FSS director at resonant frequency of 3.7 GHz. It possesses an impedance bandwidth of 810 MHz (3.38 GHz-4.19 GHz) with $|S_{11}| < -10$ dB and a gain at 0 degrees of 3.05 dBi. Fig. 18(c) demonstrates that the antenna with FSS director has an impedance bandwidth of 2.12 GHz (4.73 GHz-6.85 GHz) with $|S_{11}| < -10$ dB at the resonant frequency of 5.2 GHz and a gain of 3.72 dBi at 0 degrees. According to the results, it was determined that the antenna with and without FSS director can operate at the same resonant frequency of 1.8 GHz, 3.7 GHz, and 5.2 GHz. Figures 19(a) to (c) depict the simulation outcomes of the magnitude of the S_{11} parameter while rotating around the z-axis at frequencies of 1.8 GHz, 3.7 GHz, and 5.2 GHz. The findings suggest that there are negligible coupling effects observed at the frequency of 1.8GHz when the angle is rotated around the z-axis. This absence of impact on the impedance bandwidth at this frequency is noteworthy.

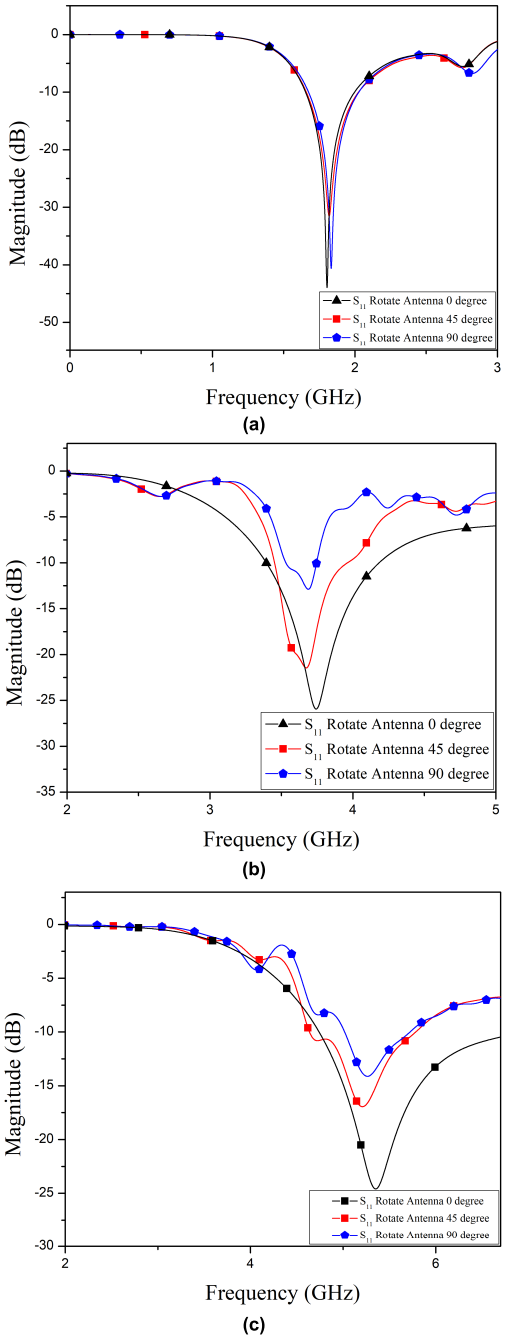

FIGURE 19. The simulation result of $|S_{11}|$ as varying rotation angle around z-axis.

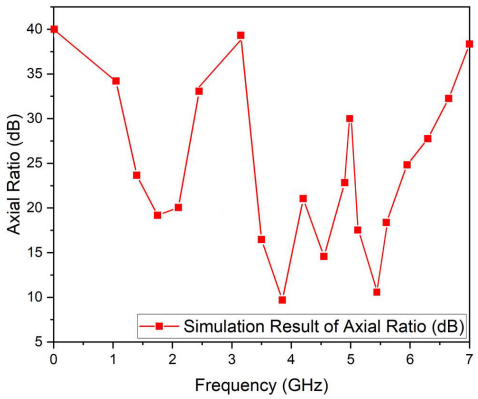

FIGURE 20. The simulation result of axial ratio over the operating frequency.

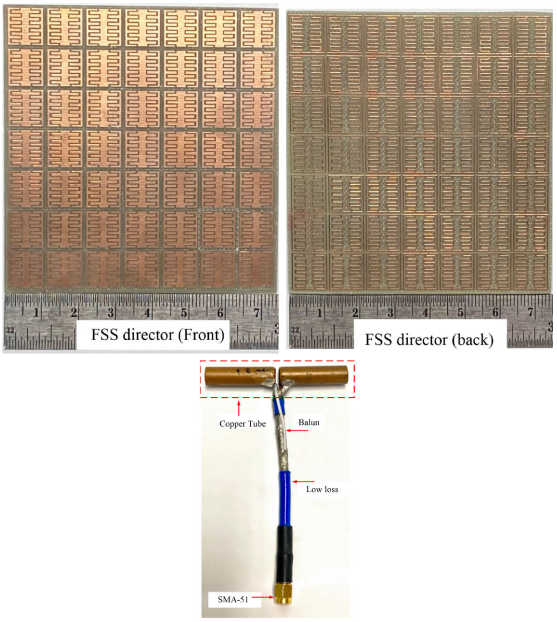

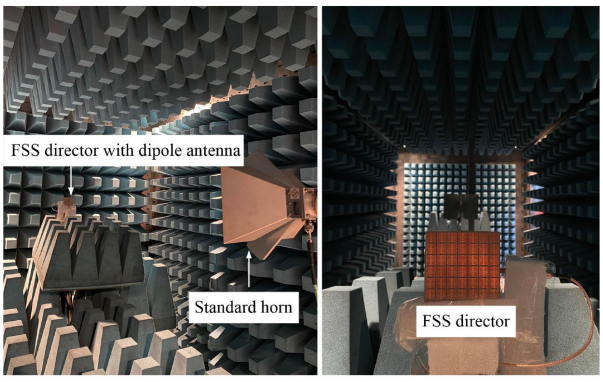

FIGURE 21. The prototype antenna with FSS director (a) configuration and (b) measured in the anechoic chamber room.

However, at frequencies of 3.7 GHz and 5.2 GHz, rotating the angle around the z-axis results in a coupling effect. This effect is manifested in the impedance bandwidth, which is influenced by the reflection and transmission effect, as illustrated in Fig. 5. Furthermore, the proposed FSS director can transmit electromagnetic waves with the antenna effectively and increase the antenna gain. The axial ratio (AR) depicted in Fig. 20 exhibits a value exceeding 10 dB throughout all frequency bands of operation. It is stated that linear polarization is a property of the FSS director. The fabrication procedure and measurement will be discussed in the following section.

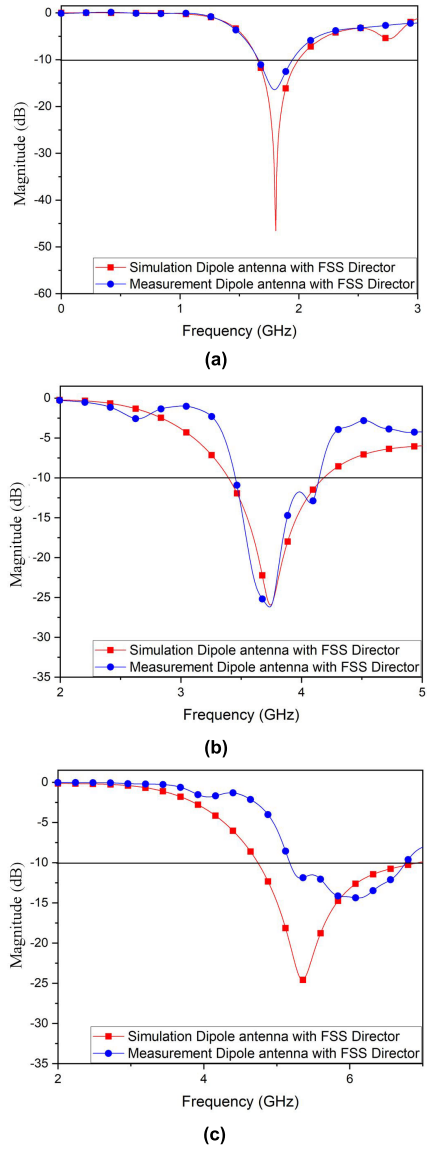

FIGURE 22. The measured reflection coefficient of the antenna with FSS director at the frequency of (a) 1.8 GHz, (b) 3.7 GHz, and (c) 5.2 GHz.

IV. MEASUREMENT RESULTS

The FSS director designed in the preceding section will be fabricated the prototype director using FR-4 printed circuit board with a dielectric constant (ε_r) of 3.2, a substrate thickness of 1.6 mm, a conductor thickness of 0.035 mm, and a loss tangent (tanδ) of 0.04. The prototype director is manufactured using an LPKF milling machine, and its dimensions are 73.48 mm × 77.38 mm. Then, each single-frequency dipole antenna designed in the preceding simulation will be manufactured at the resonant frequency of 1.8 GHz, 3.7 GHz, and 5.2 GHz, respectively. Each prototype antenna will be constructed by connecting a copper tube to a low-loss RG-45 cable; additionally, a balun circuit will be utilized to compensate for the current between the unbalanced and balanced lines. The prototype of antenna and FSS director depicts in Fig. 21(a). The prototype antenna with FSS director will be measured and evaluated the antenna characteristic in the Anechoic Chamber Room as shown in Fig. 21(b). The antenna was positioned behind the director at a distance of 15.70 mm, 11.24 mm, and 8.46 mm for resonant frequencies of 1.80 GHz, 3.70 GHz, and 5.20 GHz, respectively. Figs. 22 (a) to (c) depict a comparison between the simulated and measured results of the dipole antenna with the proposed FSS director. The results demonstrate that the antenna's reflection coefficient $|S_{11}|$ is less than -10 dB at all frequencies examined. The impedance bandwidth for the 1.8 GHz frequency is 290 MHz (1.66 GHz – 1.95 GHz), whereas the impedance bandwidth for the 3.7 GHz frequency is 700 MHz (3.45 GHz-4.15 GHz), and the impedance bandwidth is 1.41 GHz (4.52 GHz-5.93 GHz) at 5.2 GHz. Comparing simulation and measurement results reveals that the impedance bandwidth is near to the simulated result; although, there may be a minor shift in the resonance frequency range of 5.2 GHz due to the fabrication process of the prototype antenna with FSS director, its frequency and bandwidth remain within the required range. Figs. 23 (a) to (c) depict the measured radiation patterns of the antenna with the FSS director at the resonant frequency of 1.8 GHz, 3.7 GHz, and 5.2 GHz, respectively. At all resonant frequencies, it appears that radiation patterns are bidirectional in XZ-planes and omnidirectional in YZ-planes. Although, the cross polarization increases at the higher resonant frequency due to the higher order mode of the director, the direction of radiation pattern still propagates the electromagnetic wave effectively at 0 degree in XZ and YZ-planes. Moreover, the measured gains of the antenna with the FSS director are 3.05 dBi, 2.98 dBi, and 3.12 dBi at frequencies of 1.8 GHz, 3.7 GHz, and 5.2 GHz, respectively. The results indicate that the proposed FSS director has successfully performed the responsibility of transmitting electromagnetic waves and regulating the direction of the beam towards 0 degrees across all frequencies of resonance. The study indicates that the proposed FSS exhibits superior beam direction control compared to the prior FSS configuration as reported in [22]. Because the unit cell analyzed in [22] displays an uneven distribution of electric current within the unit cell, leading to a misalignment of the wave propagation pattern at a 0-degree angle. The proposed unit cell has been specifically designed to exhibit a symmetrical configuration. As a result, the current distribution demonstrates a symmetrical pattern, which results in the clear transmission of waves with zero degrees of propagation. Moreover, the proposed unit cell structure has been designed with the aim of improving the capacitance values of C_c and C_g. The augmentation of C_g will enhance the slow wave in comparison to the traditional configuration. Additionally, the capacitance value of C_c not only improves the efficiency of slow wave propagation, but it can also serve as an adjustment tool for fine-tuning the second and third resonant frequencies in comparison to [22]. The tuning effect that has been observed in [22] does not offer adequate evidence to support the concept of fine-tuning.

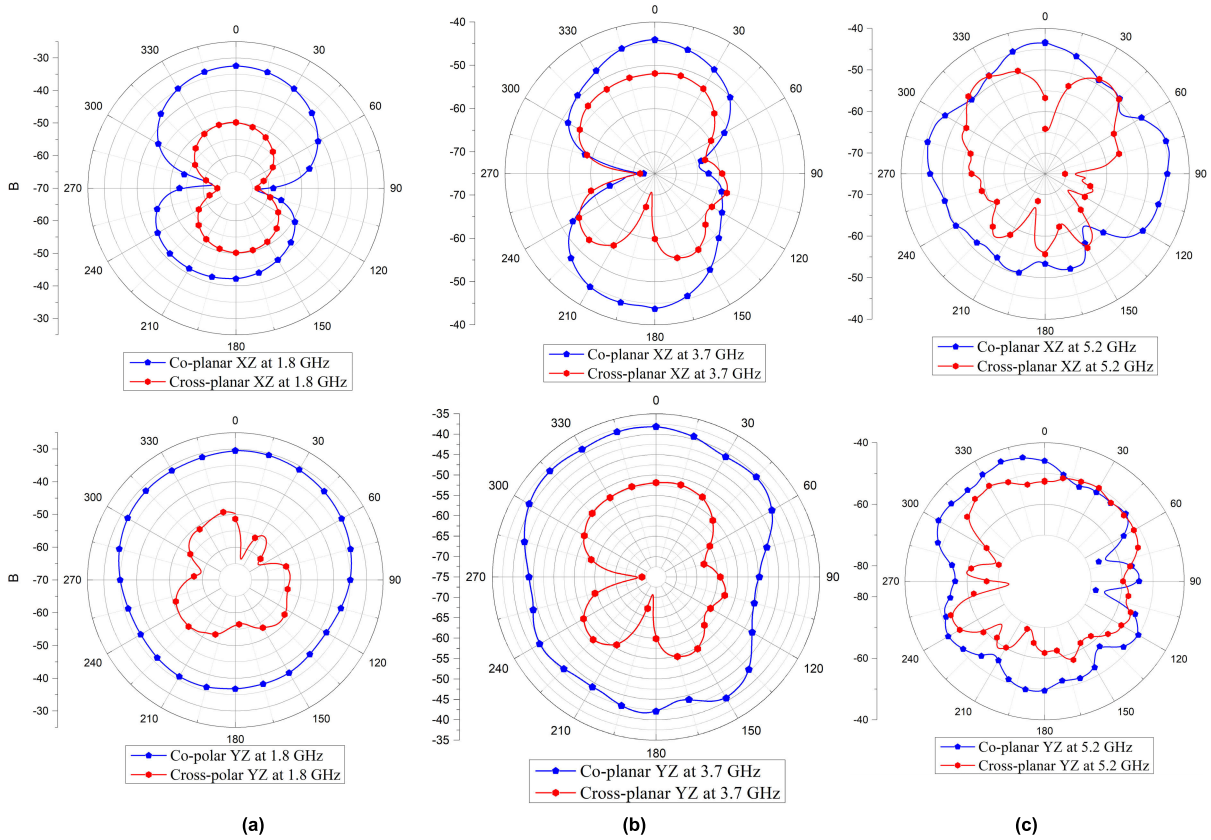

FIGURE 23. The measured radiation patterns of the antenna with FSS director at (a) 1.8 GHz, (b) 3.7 GHz, and (c) 5.2 GHz.

Modifying the capacitive value of C_i has a significant and immediate effect on the frequency, which presents difficulties in efficiently controlling the resonant frequency. Therefore, it is imperative that the capacitive value of C_c be designed to effectively mitigate this limitation. As the result, the proposed FSS director can enhance the conventional antenna gain and make fine-tuning the resonant frequency easier in order to support the wireless communication system's operation at the specified frequency.

V. CONCLUSION

This article describes a miniaturized multiband FSS director that utilizes a dual-layer FSS director. Applying the Interdigital CPW method and a square loop resonator with a double meander line, the unit cell is constructed. The techniques permit the first- through third-order resonant frequencies to occur at 1.80 GHz, 3.70 GHz, and 5.20 GHz, respectively. Consequently, it has been determined that increasing the capacitive load of the interdigital technique applied to a transmission line produces a slow wave, resulting in a substantially shorter transmission line. In addition, the capacitive value of the double meander line will significantly increase the capacitive value of the transmission line, resulting in an increase in the slow-wave value and a smaller double-layer FSS unit cell structure at resonant frequencies than the standard unit cell. However, the conventional unit cell structure is designed for a wavelength of about $\lambda/2$, whereas the proposed unit cell can reduce the dimension to about $\lambda/8$. Moreover, the capacitive load affects the frequency shift across all frequency ranges. This capacitive load has an effect on the first and third-order resonance frequencies, but its effect on the second-order frequency is the most significant. Thus, the proposed structure's first-order resonance frequency is determined by the transmission line and square loop resonator structures. The capacitive load controls the resonant frequencies of the second and third order. Especially at second-order resonance frequencies, where a substantial movement in the resonant frequency range occurs, a step-impedance technique must be applied to the transmission line to achieve the desired resonance frequency control. When the proposed unit cell is arranged as an FSS director in an array, the overall dimensions of the structure are drastically reduced. Upon applying the FSS director to dipole antennas, it was discovered that the impedance matching was less than -10 dB at all resonant frequencies within the operating frequency range. It transmits effectively, resulting in antenna gains of 3.05 dBi, 2.98 dBi, and 3.12 dBi at 1.8 GHz, 3.7 GHz, and 5.2 GHz, respectively. In addition, at the resonant frequencies, the radiation patterns of the antenna with the proposed FSS director are bidirectional and omnidirectional in the XZ and YZ planes. The proposed FSS director can be utilized in a number of wireless communication system applications, such as a protective

casing for base station antennas, materials designed to avoid detection during radio frequency interference, etc. Comparing the reference research to the research presented in Table 3, it is determined that the proposed FSS unit cell has the smallest dimensions and multiple resonant frequencies. The advantage of the FSS director is that it applies to the beam-steering phased array antenna system, MIMO system, and cube satellite.

REFERENCES

[1] S. E. Mendhe and Y. P. Kosta, "Metamaterial properties and applications," *Int. J. Inf. Technol. Knowl. Manag.*, vol. 4, no. 1, pp. 85–89, 2011.

[2] Y. Tian, G. Wen, and Y. Huang, "Multiband negative permittivity metamaterials and absorbers," *Adv. OptoElectron.*, vol. 2013, pp. 1–7, Jul. 2013, doi: 10.1155/2013/269170.

[3] D. Marathe and K. Kulat, "A compact triple-band negative permittivity metamaterial for C, X-band applications," *Int. J. Antennas Propag.*, vol. 2017, pp. 1–12, Jan. 2017, doi: 10.1155/2017/7515264.

[4] W. Kamonsin, P. Krachodnok, P. Chomtong, and P. Akkaraekthalin, "Dual-band metamaterial based on Jerusalem cross structure with interdigital technique for LTE and WLAN systems," *IEEE Access*, vol. 8, pp. 21565–21572, 2020, doi: 10.1109/ACCESS.2020.2968563.

[5] L. Yang, M. Fan, F. Chen, J. She, and Z. Feng, "A novel compact electromagnetic-bandgap (EBG) structure and its applications for microwave circuits," *IEEE Trans. Microw. Theory Techn.*, vol. 53, no. 1, pp. 183–190, Jan. 2005.

[6] L. Li, Q. Chen, Q. Yuan, C. Liang, and K. Sawaya, "Surface-wave suppression band gap and plane-wave reflection phase band of mushroomlike photonic band gap structures," *J. Appl. Phys.*, vol. 103, no. 2, pp. 1–8, Jan. 2008, doi: 10.1063/1.2832401.

[7] L. Peng, C.-L. Ruan, and J. Xiong, "Compact EBG for multi-band applications," *IEEE Trans. Antennas Propag.*, vol. 60, no. 9, pp. 4440–4444, Sep. 2012, doi: 10.1109/TAP.2012.2207036.

[8] A. Yadav, S. Goyal, T. Agrawal, and R. P. Yadav, "Multiband antenna for Bluetooth/ZigBee/Wi-Fi/WiMAX/WLAN/X-band applications: Partial ground with periodic structures and EBG," *Nature Commun.*, vol. 11, no. 4186, p. 21, Aug. 2020, doi: 10.1109/ICRAIE.2016.7939576.

[9] Y. Cheon, J. Lee, and J. Lee, "Quad-band monopole antenna including LTE 700 MHz with magneto-dielectric material," *IEEE Antennas Wireless Propag. Lett.*, vol. 11, pp. 137–140, 2012, doi: 10.1109/LAWP.2012.2184517.

[10] C. Niamien, S. Collardey, A. Sharaiha, and K. Mahdjoubi, "Compact expressions for efficiency and bandwidth of patch antennas over lossy magneto-dielectric materials," *IEEE Antennas Wireless Propag. Lett.*, vol. 10, pp. 63–66, 2011, doi: 10.1109/LAWP.2011.2107493.

[11] B.-Y. Park, M.-H. Jeong, and S.-O. Park, "A magneto-dielectric handset antenna for LTE/WWAN/GPS applications," *IEEE Antennas Wireless Propag. Lett.*, vol. 13, pp. 1482–1485, 2014, doi: 10.1109/LAWP.2014.2342256.

[12] B. A. Munk, *Frequency-Selective Surface Theory and Design*. New York, NY, USA: Wiley, 2000.

[13] M.-J. Huang, M.-Y. Lv, J. Huang, and Z. Wu, "A new type of combined element multiband frequency selective surface," *IEEE Trans. Antennas Propag.*, vol. 57, no. 6, pp. 1798–1803, Jun. 2009, doi: 10.1109/TAP.2009.2019910.

[14] R. V. S. R. Krishna and R. Kumar, "Slotted ground microstrip antenna with FSS reflector for high-gain horizontal polarisation," *Electron. Lett.*, vol. 51, no. 8, pp. 599–600, Apr. 2015, doi: 10.1049/el.2015.0339.

[15] A. A. Omar and Z. Shen, "Multi-band second-order bandstop frequency selective structure with controllable band ratios," in *Proc. IEEE Int. Symp. Antennas Propag. USNC/URSI Nat. Radio Sci. Meeting*, Jul. 2015, pp. 1260–1261, doi: 10.1109/APS.2015.7305019.

[16] A. G. Neto, A. G. D. Assunção, J. C. E. Silva, J. D. N. Cruz, J. B. de Oliveira Silva, and N. J. Pereira de Lyra Ramos, "Multiband frequency selective surface with open Matryoshka elements," in *Proc. 9th Eur. Conf. Antennas Propag. (EuCAP)*, Apr. 2015, pp. 1–5.

[17] M. Yan, J. Wang, H. Ma, M. Feng, Y. Pang, S. Qu, J. Zhang, and L. Zheng, "A tri-band, highly selective, bandpass FSS using cascaded multilayer loop arrays," *IEEE Trans. Antennas Propag.*, vol. 64, no. 5, pp. 2046–2049, May 2016.

[18] B. Döken and M. Kartal, "Easily optimizable dual-band frequency-selective surface design," *IEEE Antennas Wireless Propag. Lett.*, vol. 16, pp. 2979–2982, 2017, doi: 10.1109/LAWP.2017.2756118.

[19] N. Liu, X. Sheng, J. Fan, Y. Wang, and D. Guo, "Reconfigurable frequency selective surface with multiband characteristic," in *Proc. Int. Conf. Electromagn. Adv. Appl. (ICEAA)*, Sep. 2017, pp. 897–899, doi: 10.1109/ICEAA.2017.8065398.

[20] M. Mantash, A. Kesavan, and T. A. Denidni, "Beam-tilting endfire antenna using a single-layer FSS for 5G communication networks," *IEEE Antennas Wireless Propag. Lett.*, vol. 17, no. 1, pp. 29–33, Jan. 2018, doi: 10.1109/LAWP.2017.2772222.

[21] A. Chatterjee and S. K. Parui, "Frequency-dependent directive radiation of monopole-dielectric resonator antenna using a conformal frequency selective surface," *IEEE Trans. Antennas Propag.*, vol. 65, no. 5, pp. 2233–2239, May 2017, doi: 10.1109/TAP.2017.2677914.

[22] P. Chomtong, P. Krachodnok, K. Bandudej, and P. Akkaraekthalin, "A multiband FSS director using aperture interdigital structure for wireless communication systems," *IEEE Access*, vol. 10, pp. 11206–11219, 2022, doi: 10.1109/ACCESS.2022.3144642.

[23] G. Das, A. Sharma, R. K. Gangwar, and M. S. Sharawi, "Performance improvement of multiband MIMO dielectric resonator antenna system with a partially reflecting surface," *IEEE Antennas Wireless Propag. Lett.*, vol. 18, no. 10, pp. 2105–2109, Oct. 2019, doi: 10.1109/LAWP.2019.2938004.

[24] M. E. de Cos and F. Las-Heras, "Dual-band uniplanar CPW-fed monopole/EBG combination with bandwidth enhancement," *IEEE Antennas Wireless Propag. Lett.*, vol. 11, pp. 365–368, 2012, doi: 10.1109/LAWP.2012.2192493.

[25] J. Coonrod, "Comparing micostrip and CPW performance," *Microw. J.*, vol. 55, no. 7, pp. 74–82, 2012.

[26] M. Joodaki and M. Rezaee, "Coplanar waveguide (CPW) loaded with an electromagnetic bandgap (EBG) structure: Modeling and application to displacement sensor," *IEEE Sensors J.*, vol. 16, no. 9, pp. 3034–3040, May 2016, doi: 10.1109/JSEN.2016.2527499.

[27] P. Jirasakulporn, P. Chomtong, K. Bandudej, and P. Akkaraekthalin, "A compact triple band EBG using interdigital coplanar waveguide structure for antenna gain enhancement," *Int. J. Antennas Propag.*, vol. 2020, pp. 1–18, Dec. 2020, doi: 10.1155/2020/2856807.

[28] R. S. Beeresha, A. M. Khan, and R. H. V. Manjunath, "Design and optimization of interdigital capacitor," in *Proc. ICRIET*, 2016, pp. 73–78.

[29] S. Meesomklin, P. Chomtong, and P. Akkaraekthalin, "A compact multiband BPF using step-impedance resonators with interdigital capacitors," *Radioengineering*, vol. 25, no. 2, pp. 258–267, Apr. 2016, doi: 10.13164/re.2016.0258.

[30] T. Zhou, Y. Cao, and Z. Cheng, "Compact multiband interdigital-coupled-fed planar antenna with stepped-impedance structures for mobile handsets," *Int. J. Antennas Propag.*, vol. 2017, pp. 1–8, Jan. 2017, doi: 10.1155/2017/7435834.

[31] F. Xu, L. Li, K. Wu, S. Delprat, and M. Chaker, "Application of FDFD algorithm combined with shift-and-invert Arnoldi technique in bilateral interdigital coplanar waveguide slow wave structure," in *IEEE MTT-S Int. Microw. Symp. Dig.*, Jun. 2006, pp. 1025–1028, doi: 10.1109/MWSYM.2006.249918.

[32] F. Xu, L. Li, K. Wu, S. Delprat, and M. Chaker, "Parameter extraction of interdigital slow-wave coplanar waveguide circuits using finite difference frequency domain algorithm," *Int. J. RF Microw. Comput.-Aided Eng.*, vol. 18, no. 3, pp. 250–259, 2008, doi: 10.1002/mmce.20284.

[33] W. Cheng, L. Li, G. Liu, Y. Xiao, Z.-Y. Wang, and J.-X. Yang, "An interdigital capacitor loaded slot antenna with compact size," *Prog. Electromagn. Res. Lett.*, vol. 64, pp. 15–19, 2016, doi: 10.2528/PIERL16091201.

[34] M. Makimoto and S. Yamashita, "Bandpass filters using parallel coupled stripline stepped impedance resonators," *IEEE Trans. Microw. Theory Techn.*, vol. MTT-28, no. 12, pp. 1413–1417, Dec. 1980, doi: 10.1109/TMTT.1980.1130258.

[35] J.-T. Kuo and E. Shih, "Microstrip stepped impedance resonator bandpass filter with an extended optimal rejection bandwidth," *IEEE Trans. Microw. Theory Techn.*, vol. 51, no. 5, pp. 1554–1559, May 2003, doi: 10.1109/TMTT.2003.810138.

[36] A. Munir, "Equivalent circuit analysis of square-loop-resonator BPF with cross-shaped I/O coupling for X-band frequency application," in *Proc. Int. Conf. Control, Electron., Renew. Energy Commun. (ICCREC)*, Sep. 2017, pp. 66–69, doi: 10.1109/ICCEREC.2017.8226670.

[37] G. Sung, K. Sowerby, M. Neve, and A. Williamson, "A frequency-selective wall for interference reduction in wireless indoor environments," *IEEE Antennas Propag. Mag.*, vol. 48, no. 5, pp. 29–37, Oct. 2006, doi: 10.1109/MAP.2006.277152.
[38] Y. Xu and M. He, "Design of multilayer frequency-selective surfaces by equivalent circuit method and basic building blocks," *Int. J. Antennas Propag.*, vol. 2019, pp. 1–13, Aug. 2019, doi: 10.1155/2019/9582564.
[39] R. V. Gatti and R. Rossi, "A novel meander-line polarizer modeling procedure and broadband equivalent circuit," *IEEE Trans. Antennas Propag.*, vol. 65, no. 11, pp. 6179–6184, Nov. 2017, doi: 10.1109/TAP.2017.2754471.
[40] B. Moradi, R. Fernández-García, and I. Gil, "Meander microwave bandpass filter on a flexible textile substrate," *Electronics*, vol. 8, no. 1, pp. 1–9, Dec. 2018.

P. CHOMTONG (Member, IEEE) received the M.Eng. and Ph.D. degrees in electrical engineering from the King Mongkut's University of Technology North Bangkok (KMUTNB), Thailand, in 2006 and 2011, respectively. In 2012, he joined the Department of Teacher Training in Electrical Engineering, KMUTNB, as an Instructor. His current research interests include passive and active microwave circuits, wideband and multiband antennas, and telecommunication systems.

N. SOMJIT (Senior Member, IEEE) received the Dipl.-Ing. (M.Sc.) degree from the Dresden University of Technology (TU Dresden), Dresden, Germany, in 2005, and the Ph.D. degree from the KTH Royal Institute of Technology, Stockholm, Sweden, in 2012. Then, he returned to TU Dresden, to lead the Research Team in Microsensors and MEMS ICs for the Chair for Circuit Design and Network Theory. In 2013, he was appointed as a Lecturer (an Assistant Professor) with the School of Electronic and Electrical Engineering, University of Leeds, Leeds, U.K., where he is currently an Associate Professor. Since 2022, he has been leading a research team as an Adjunct Faculty Member with the Micro and Nanosystems Department, KTH Royal Institute of Technology. His main research focuses on integrated smart high-frequency components, sustainable micro and nanosystems, and low-cost microfabrication processes. He was appointed as a member of the Engineering, Physical and Space Science Research Panel, British Council, in 2014. He was a recipient of the Best Paper Award (EuMIC Prize) at the European Microwave Week, in 2009. He received the Graduate Fellowship from the IEEE Microwave Theory and Techniques Society (MTT-S), in 2010 and 2011, and the IEEE Doctoral Research Award from the IEEE Antennas and Propagation Society, in 2012. In 2016, he was the Chair of the Student Design Competition for the European Microwave Week. In 2018, he was appointed as an Associate Editor of *IET Electronics Letters*.

P. KRACHODNOK (Member, IEEE) received the M.Eng. degree in electrical engineering from Chulalongkorn University (CU), Thailand, in 2001, and the Ph.D. degree in telecommunication engineering from the Suranaree University of Technology (SUT), Thailand, in 2008. Since 2001, she has been with the School of Telecommunication Engineering, SUT. She has experience and an expert in electromagnetic theory, microwave engineering, and antenna engineering.

C. MAHATTHANAJATUPHAT (Member, IEEE) received the M.Eng. degree from the University of Applied Sciences Rosenheim, Germany, in 2003, and the Ph.D. degree from the King Mongkut's University of Technology North Bangkok (KMUTNB), Thailand, in 2009. In 2017, he was appointed as a Lecturer (an Associate Professor) with the Department of Electrical Engineering, KMUTNB. His main research interests include the designing of small antennas, using the fractal geometry and digital signal processing for communication applications.

S. TAWATCHAI received the bachelor's degree in aeronautical electronics engineering from the Civil Aviation Training Center (CATC), Thailand, in 2023. His research interests include high-frequency and millimeter wave.

P. AKKARAEKTHALIN (Member, IEEE) received the B.Eng. and M.Eng. degrees in electrical engineering from the King Mongkut's University of Technology North Bangkok (KMUTNB), Thailand, in 1986 and 1990, respectively, and the Ph.D. degree from the University of Delaware, Newark, USA, in 1998. From 1986 to 1988, he was with the Microtek Laboratory, Thailand. In 1988, he joined the Department of Electrical Engineering, KMUTNB. His current research interests include passive and active microwave circuits, wideband and multiband antennas, and telecommunication systems. He is a member of IEICE Japan and ECTI Thailand. He was the Chairperson of the IEEE MTT/AP/ED Thailand Joint Chapter, from 2007 to 2008, and the President of the ECTI Association, from 2014 to 2015. He is currently the Head of the Senior Research Scholar Project of Thailand Research Fund (TRF).